# Synthesis of 2D Solid-Solution (NbyV<sub>2-y</sub>) $CT_x$ MXenes and Their Transformation into Oxides for Energy Storage

Marcelo A. Andrade<sup>1,2</sup>, Timofey Averianov<sup>1</sup>, Christopher E. Shuck<sup>2</sup>, Kateryna Shevchuk<sup>2</sup>, Yury Gogotsi<sup>2</sup>, Ekaterina Pomerantseva<sup>1</sup>\*

<sup>2</sup>A.J. Drexel Nanomaterials Institute and Department of Materials Science and Engineering, Drexel University, Philadelphia, PA 19104, USA.

**Keywords:** bilayered vanadium oxide; niobium oxide; solid-solution MXenes; energy storage; Li-ion batteries

#### **Abstract**

Vanadium and niobium oxides have been identified as promising electrodes for electrochemical energy storage applications as their constituent transition metals can undergo multiple reduction steps leading to high specific capacities during cycling. MXenes are attractive precursors for these compounds due to their tunable compositions and 2D nanoscale morphology. Herein, we demonstrate the synthesis of a wide range of solid-solution (Nb<sub>v</sub>V<sub>2</sub>y)AlC MAX phases, their chemical etching to produce (Nb<sub>y</sub>V<sub>2-y</sub>)CT<sub>x</sub> MXenes, and the subsequent oxidation of MXenes to form respective oxides. We show that formation of solid solutions facilitated the etching kinetics of MAX phase powder and accelerated MXene formation compared to pure vanadium and niobium carbides. Oxidation of V<sub>2</sub>CT<sub>x</sub> and Nb<sub>2</sub>CT<sub>x</sub> produced bilayered vanadium oxide (BVO) with a crumpled nanosheet morphology and nanostructured amorphous Nb<sub>2</sub>O<sub>5</sub> (nANO) nanospheres, respectively. For oxides derived from the solid-solution MXenes, SEM imaging revealed the growth of nANO on the surface of BVO nanosheets. Electrochemical cycling of  $(Nb_{\nu}V_{2-\nu})CT_x$ -derived oxides in Li-ion cells revealed varying intercalation-like behavior with electrode derived from  $V_2CT_x$  showing redox processes and nANO exhibiting pseudocapacitive response. The CV curves of solid-solution MXenederived oxides demonstrated primarily BVO/nANO composite-like behavior, with key exceptions. The cells containing  $Nb_{0.25}V_{1.75}CT_x$ -derived oxide showed a large capacity of 296.8 mAh·g<sup>-1</sup> driven by significant electrochemical activity at all potentials along the sweep possibly stemming from niobium doping into BVO structure. The Nb<sub>1.00</sub>V<sub>1.00</sub>CT<sub>x</sub>-derived oxide

<sup>&</sup>lt;sup>1</sup>Materials Electrochemistry Group, Department of Materials Science and Engineering, Drexel University, Philadelphia, PA 19104, USA.

<sup>\*</sup> Corresponding Author: ep423@drexel.edu

electrode delivered specific capacity of 297.8 mAh·g<sup>-1</sup> with contributions from both BVO and nANO phases. The improved electrochemical stability of (Nb<sub>1.00</sub>V<sub>1.00</sub>)CT<sub>x</sub>-derived oxide electrodes compared to an electrode prepared by physically mixing Nb<sub>2</sub>CT<sub>x</sub>-derived oxide with V<sub>2</sub>CT<sub>x</sub>-derived oxide with the same Nb:V molar ratio was attributed to the stabilizing effect of BVO/nANO heterointerface. Our work indicates that the use of solid-solution MXenes as precursors is an attractive strategy to synthesize oxides with compositions, morphologies and properties that cannot be produced otherwise.

## 1. Introduction

Nanostructured materials open a pathway to increase the electrode/electrolyte contact area and reduce diffusion distances, leading to enhanced specific capacities and improved rate capabilities for faster battery operation. Despite limitations, such as parasitic reactions caused by high surface area and overall scalability, nanostructured materials can provide improved transport of ions and electrons required for high-power energy storage devices. The developed methods for preparing nanomaterials pave a way for achieving improved electrochemical performance. Creative synthesis approaches utilizing non-traditional precursors can lead to products with superior properties. As

Layered oxides of transition metals in high oxidation states, such as niobium and vanadium, have been explored for lithium-ion battery electrodes as they can reversibly undergo multiple reduction steps by intercalation of multiple Li<sup>+</sup> ions in a single unit cell, leading to high charge storage capacities.<sup>5</sup> Specifically, bilayered vanadium oxide (BVO or δ-V<sub>2</sub>O<sub>5</sub>·nH<sub>2</sub>O<sup>6</sup>) has attracted attention as a versatile high-capacity cathode material for Li-ion and beyond Li-ion energy storage systems.<sup>7-9</sup> The high capacity of BVO (~200 mAh·g<sup>-1</sup> in the potential window of 2.0 – 4.0 V vs Li/Li<sup>+</sup>) is enabled by V<sup>5+</sup> in its structure enabling multielectron redox processes, expanded interlayer region stabilized by water pillaring, and synthetic diversity with various ionic intercalants. 10-14 On the other hand, nanostructured amorphous niobium pentoxide (nANO), Nb<sub>2</sub>O<sub>5</sub>, functions as an anode material featuring pronounced pseudocapacitive behavior, resulting in high Li<sup>+</sup> ion storage capacity (~200 mAh·g<sup>-1</sup> in the potential window of 1.0 – 3.0 V vs. Li/Li<sup>+</sup>) with high-rate capability. 15-17 Similar to BVO, nANO can be synthesized with energetically efficient sol-gel chemistries, which is vital for increasing the production of these types of metastable phases. 15, 18 However, this synthesis can be modified with the use of precursor materials that promote the formation of unique morphologies and chemistries.<sup>3, 4</sup>

MXenes are an emergent class of two-dimensional (2D) transition metal carbides, nitrides, and carbonitrides with the general formula  $M_{n+1}X_nT_x$ , where M is an early transition metal (Nb, V, Ti, etc.) X is C and/or N,  $T_x$  represents the surface functional groups (O, OH, F, etc.), and n = 1-4. Multiple transition metals can occupy M sites, leading to solid-solution MXenes with enhanced functionality. By introducing multiple transition metals at the MAX phase synthesis step, solid-solution MXenes can be produced by subsequent etching of these parent ceramic MAX phases. These solid-solution chemistries can be leveraged when using MXenes as precursors for oxide synthesis. MXenes have been previously shown to form

transition metal oxides through hydrolysis in the presence of water.  $^{26}$  Other oxidizing agents can be used to facilitate the transformation of MXenes into oxides.  $^{27}$  In particular, hydrogen peroxide has been used to dissolve and oxidize multilayer  $V_2CT_x$  MXene powder in the presence of chlorides of alkali (Li<sup>+</sup>, Na<sup>+</sup>, K<sup>+</sup>) and alkaline-earth (Mg<sup>2+</sup>, Ca<sup>2+</sup>) metal ions; subsequent hydrothermal treatment of the resulting mixture produced chemically preintercalated BVOs. The  $V_2CT_x$ -derived  $\delta$ -M<sub>x</sub> $V_2O_5$ ·nH<sub>2</sub>O (M = Li<sup>+</sup>, Na<sup>+</sup>, K<sup>+</sup>, Mg<sup>2+</sup>, Ca<sup>2+</sup>) exhibited a 2D petal-like morphology coalesced into particles with nanoflower shapes; BVOs derived from vanadium salts or orthorhombic  $\alpha$ -V<sub>2</sub>O<sub>5</sub> typically form 1D nanorods or nanobelts.  $^{28}$ ,  $^{29}$  The MXene-derived BVOs with nanoflower morphologies showed enhanced electrochemical stability in Li-ion cells as compared to the 1D BVOs derived from other precursors.  $^4$ 

Implementation of solid-solution MXenes as precursors offers a pathway to further enrich the chemical composition of MXene-derived oxides and ability to synthesize novel materials.<sup>19</sup> The multiple transition metals in solid-solution MXenes present an interesting approach to obtain materials with mixed phases or doping of one metal into another parent oxide structure. 30-32 Additionally, the 2D morphology of MXenes can lead to stabilization of 2D morphologies of oxide phases.<sup>33</sup> Solid-solution MXene-derived oxides are particularly relevant for battery materials, as they can provide more versatile structural and electrochemical properties. Husmann et al. synthesized a series of (Ti,Nb)CT<sub>x</sub> MXenes that were thermally annealed at 900 °C, producing TiO2 and Ti2Nb10O29. 30 The MXene-derived Ti2Nb10O29 is a layered oxide shown to retain its morphology from the precursor MXene and contains carbon from the incomplete oxidation process, which improved its conductivity, leading to better rate performance.<sup>30</sup> Liu et al. explored the transformation of TiNbC into niobium-doped TiO<sub>2</sub>.<sup>31</sup> Cycling in Li-ion half cells showed that the TiO<sub>2</sub> on MXene treated at 500 °C delivered the best rate and cycle life performance, as well as the smallest charge-transfer resistance.<sup>31</sup> This finding was explained by the contribution of surface charge transfer in capacitive charge storage. Yu et al. used  $V_3CrC_3T_x$  as a precursor to synthesize a Cr-substituted  $Na_3V_2(PO_4)_3$  and then investigated it as a cathode in Na-ion batteries.<sup>32</sup> The substitution of Cr changed the Na<sup>+</sup> charge storage behaviour by increasing Na<sup>+</sup> ion diffusion during cycling. This led to improved highrate performance and boosted energy density of sodium vanadium phosphates.<sup>32</sup> However, there are no reports on the transformation of Nb-V solid-solution MXenes into oxides and their subsequent electrochemistry. Our goal was to fill this gap in knowledge.

In this work,  $(Nb_yV_{2-y})CT_x$  solid-solution MXenes were produced by selective etching of Nb-V solid-solution MAX phases with controlled Nb:V ratios followed by oxidation through

a two-step process consisting of dissolution in hydrogen peroxide and recrystallization by hydrothermal treatment at 140 °C. The (Nb<sub>y</sub>V<sub>2-y</sub>)CT<sub>x</sub> MXene-derived oxides show a range of morphologies and structures between the layered BVO derived from V<sub>2</sub>CT<sub>x</sub>, to the nanostructured amorphous niobium oxide derived from Nb<sub>2</sub>CT<sub>x</sub>, and BVO/nANO nanocomposites for compositions containing both V and Nb atoms. Cycling voltammetry study of the (Nb<sub>y</sub>V<sub>2-y</sub>)CT<sub>x</sub>-derived oxide electrodes in non-aqueous Li-ion cells demonstrated that the composition variation gradually altered their charge storage properties. The advantages of using solid-solution MXenes as precursor for the synthesis of oxides are discussed by comparing electrochemical cycling of (Nb<sub>1.00</sub>V<sub>1.00</sub>)CT<sub>x</sub>-derived oxide electrodes and electrodes prepared by physically mixing Nb<sub>2</sub>CT<sub>x</sub>-derived oxide with V<sub>2</sub>CT<sub>x</sub>-derived oxide with a Nb:V molar ratio of 1:1.

## 2. Materials and Methods

## Synthesis of the solid-solution MAX Phases

(Nb<sub>y</sub>V<sub>2-y</sub>)AlC (y = 0.00, 0.25, 0.50, 0.75, 1.00, 1.25, 1.50, 1.75, and 2.00) MAX phases were synthesized using aluminum powder (Al 99.5%, -325 mesh, Alfa Aesar), graphite (C 99%, -325 mesh, Alfa Aesar), vanadium powder (V 99.5%, -325 mesh, Alfa Aesar) and niobium powder (Nb 99.8%, -325 mesh, Alfa Aesar). The powders were mixed in the 2:1.1:0.9 (M:Al:C) atomic ratio, with a total mass of 50 g. Each mixture was transferred to an individual 125 mL polypropylene jar with 100 g of yttria stabilized zirconia balls (5 mm) and ball milled at 60 RPM for 16 h.

After ball milling, the powder was passivated to avoid self-combustion by slowly reintroducing air by gradually opening the cover (4 h process). The milled powder mixtures were then transferred to alumina crucibles for pressureless sintering in a high-temperature furnace (Carbolite Gero). The tube furnace was filled with argon and kept under a constant Ar flow of ~200 cm³/min for 1 h before heating at 3 °C/min to 1550 °C, held for 2h, and cooled down to room temperature at the same rate.

The obtained bricks were milled to a fine powder using a mortar and pestle and sieved to select particles with sizes  $<40~\mu m$ . The obtained powders were washed overnight with concentrated hydrochloric acid (HCl, 36.5-38%, Fisher Chemical), (2 mL of acid per 1 g of MAX phase) to remove any residual intermetallic particles, then washed several times with sufficient DI water and dried under vacuum at room temperature. These MAX phases will be referred to as SS-MAX phases.

## Synthesis of $(Nb_{\nu}V_{2-\nu})CT_x$ MXenes

The same etching procedure was used for all compositions. The etchant was a mixture of deionized (DI) water, hydrochloric acid (HCl, 36.5-38%, Fisher Chemical), and hydrofluoric acid (HF, 48.5-51%, Acros Organics) in a 6:12:12 volume ratio (H<sub>2</sub>O:HCl:HF). 1 g of MAX phase powder slowly added to the 30 mL of etching solution under constant stirring (400 RPM) and kept at 35 °C for seven days.

After the etching was complete, the mixture was centrifuged at 3500 RPM for 5 minutes. The acidic supernatant was discarded, and the precipitated MXene was resuspended in fresh deionized water to continue washing. The washing procedure was repeated by discarding the supernatant and refilling the centrifuge tube with DI water until the pH of the solution was around 6. The solid was vacuum filtered to separate the multilayer MXenes, which were vacuum dried in a desiccator at room temperature overnight.

## Synthesis of solid-solution MXene-derived oxides

 $300 \,\text{mg}$  of dried multilayer MXene powder of each composition  $\{(\text{Nb}_y \text{V}_{2-y})\text{CT}_x (y=0.00, 0.25, 0.50, 0.75, 1.00, 1.25, 1.50, 1.75, and 2.00)\}$  was dispersed in 30 mL of DI water under constant stirring of 300 RPM at room temperature. 2 mL of hydrogen peroxide (30 wt. %, Fisher Scientific) was added, and the reacting mixture was kept stirring for 5 h. The supernatant solution was collected, avoiding the residual precipitate left at the bottom, equally distributed into two 23 mL Teflon liners, placed inside stainless steel autoclaves (Parr Instruments Company), and hydrothermally treated at 140 °C for 24 h. After the hydrothermal treatment, the product was collected by vacuum filtration and washed thoroughly with DI water. The obtained solid-solution MXene-derived oxides (SS-MXene-dOX or (Nb<sub>y</sub>V<sub>2-y</sub>)CT<sub>x</sub>-dOX) were dried at 105 °C overnight. A physical mixture of V<sub>2</sub>CT<sub>x</sub>-dOX and Nb<sub>2</sub>CT<sub>x</sub>-dOX with V:Nb molar ratio of 1:1, denoted V<sub>2</sub>CT<sub>x</sub>-dOX/Nb<sub>2</sub>CT<sub>x</sub>-dOX-1:1, was prepared by grinding appropriate amounts of V<sub>2</sub>CT<sub>x</sub>-dOX and Nb<sub>2</sub>CT<sub>x</sub>-dOX in a mortar with pestle and used as a reference electrode in electrochemical testing.

## **Materials Characterization**

X-ray diffraction (XRD) was used to characterize the phase composition and unit cell parameters of the synthesized materials. A Rigaku MiniFlex powder X-ray diffractometer equipped with a Cu source with  $\lambda_{K\alpha}$ = 1.54 Å was used, with a step size of 0.02° (20) and a scan

speed of 0.7 °/min. d-spacing was determined using Bragg's law from the position of (002) or (001) peaks in the XRD patterns of MXenes and BVO, respectively.

Scanning electron microscopy (SEM) images were obtained using a Zeiss Supra 50VP scanning electron microscope, using a low-energy electron beam (~5 keV) and in-lens and SE2 detectors. The materials were covered with sputtering a thin layer (~5 nm) of platinum metal.

Raman spectroscopy analysis was performed using a Renishaw inVia Raman spectrometer (Gloucestershire, UK) instrument. We used a 633 nm He-Ne laser with 1200 line/mm grating to obtain the MAX phase spectra and a 514 nm Ar laser with 1800 line/mm grating to acquire the MXene and MXene-derived oxide spectra. The excitation intensity used was 4.06 mW  $\times$ 50% at 633 nm and 1.47 mW  $\times$ 10% at 514 nm, as MAX phases are less prone to photodecomposition. A  $\times$ 63 63x objective (numerical aperture (NA) = 0.7) and 120 s acquisition time were used for MAX phase and MXene spectra tests, and a  $\times$ 20 objective (NA = 0.4) and 10 s acquisition time were used for MXene-derived oxide spectra tests.

Differential thermal analysis (DTA)/thermogravimetric analysis (TGA) was used to determine MAX phase stability under air using a TA Instruments Discovery SDT 650 Simultaneous DTA/TGA analyzer. DTA/TGA curves were collected under constant air flow of 100 mL/min from room temperature to 1450 °C at a heating rate of 20 °C/min.

## Electrode fabrication and electrochemical testing

The SS-MXene-dOX powders were dried at 200 °C under vacuum following the procedure established for hydrated oxides.<sup>34</sup> Electrodes were made with a mixture of 70 wt.% active mass, 20 wt.% acetylene carbon black (Alfa Aesar, 99.9+%) and 10 wt.% of poly(vinylidene fluoride) (PVDF) (Kynar Flex, Arkema, USA) powder. Active materials include the SS-MXene-dOX, as well as the prepared 1:1 physical mixture described above. The slurry was prepared in a dispersion of N-methyl-2-pyrrolidone (NMP). The mixture was homogenized using a Flacktek SpeedMixer at 3000 RPM for 30 seconds, forming a viscous black slurry. Casting was performed using a micrometer film applicator, with controlled thickness, over Al foil, and then the case electrode film was dried in a vacuum oven at 105 °C overnight. The 12 mm disk electrodes were punched out of the electrode film followed by another drying step in a vacuum oven at 105 °C overnight.

The dried electrode disks were transferred to an argon-filled glove box for the 2016-type coin cells assembly, using a two-electrode configuration with lithium metal as the counter and reference electrodes. The cells were assembled with two spacers, using one Celgard 3501 disk as a separator and LP40 electrolyte (Gotion, 1M LiPF<sub>6</sub> in a 1:1 vol. mixture of ethylene

carbonate (EC)/diethyl carbonate (DEC)). All cells were cycled in a voltage window of 1.0 – 4.0 V vs. Li/Li<sup>+</sup>. Cyclic voltammograms were collected at a scan rate of 0.1 mV·s<sup>-1</sup> using a BioLogic VP3 potentiostat. Galvanostatic charge/discharge cycling was performed at a current rate of 20 mA·g<sup>-1</sup> using an Arbin Laboratory Battery Tester.

## 3. Results and Discussion

The synthesized MAX (Nb<sub>y</sub>V<sub>2-y</sub>)AlC phases with controlled Nb:V ratio (y= 0.00, 0.25, 0.50, 0.75, 1.00, 1.25, 1.50, 1.75, and 2.00) were etched to create solid solution MXenes as precursors, which were then transformed to oxides using  $H_2O_2$ -initiated oxidation followed by the hydrothermal treatment, as schematically shown in **Figure 1**.

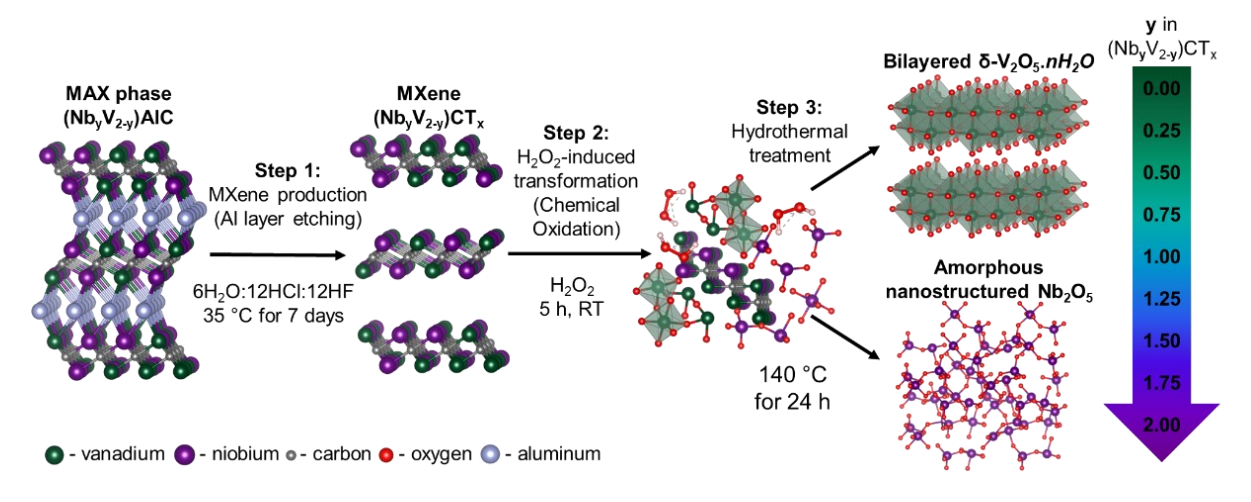


**Figure 1.** Schematic flowchart of the experimental synthesis procedure: from MAX, to MXene, to oxides.

The XRD patterns of  $(Nb_yV_{2-y})AlC$  (y = 0.00, 0.25, 0.50, 0.75, 1.00, 1.25, 1.50, 1.75, and 2.00) MAX phase powders (**Figure S1** in **Supporting Information**) reveal a linear change of *d*-spacing, related to a shift in (002) and (110) peaks towards higher *d*-spacings as the vanadium in the V<sub>2</sub>AlC is substituted with niobium, indicating that both the *a*- and *c*-lattice parameters linearly vary with composition (**Table S1** in **Supporting Information**). The change in *d*-spacings and unit cell parameters is attributed to the larger atomic radius of niobium (145 pm) compared to the radius of vanadium (135 pm). This trend confirms the formation of homogeneous solid-solution phases, with uniform distribution of both transition metals through the MAX phase structure.<sup>25</sup>

The Raman spectra of the  $(Nb_yV_{2-y})AlC$  MAX phases (**Figure S2** in **Supporting Information**) also show a trend in band positions as the composition changes. The Raman spectra of the SS Nb-V MAX phases  $(Nb_yV_{2-y})AlC$  (y = 0.25, 0.50, 0.75, 1.00, 1.25, 1.50, and

1.75) are reported for the first time. In  $V_2AlC$  spectra the peak at 155 cm<sup>-1</sup> corresponds to  $E_{2g}$  in-plane vibration of V and Al atoms. The peaks at 255 cm<sup>-1</sup> and 359 cm<sup>-1</sup> are caused by  $E_{2g}$  in-plane and  $A_{1g}$  out-of-plane vibrations of V atoms.<sup>35</sup> The position of Nb<sub>2</sub>AlC peaks are close to theoretical calculations reported by Lin et al.<sup>36</sup>  $E_{2g}$  in-plane vibration of Nb and Al atoms is located at 146 cm<sup>-1</sup>, the second  $E_{2g}$  mode is located at 196 cm<sup>-1</sup> and out-of-plane  $A_{1g}$  mode is located at 264 cm<sup>-1</sup>.

All peaks gradually upshift when moving from Nb to V in MAX phase composition. This trend was reported before: with the addition of heavier Nb atoms, the  $A_{1g}$  peak was observed to downshift.<sup>25</sup> The shift is attributed to the difference in bond stiffness between Al-Nb-C and Al-V-C in the MAX phase structures, as well as the mass difference between Nb and V atoms, which affects the vibrational modes. The bands around 200 cm<sup>-1</sup> are better resolved for the single-transition metal MAX phases (Nb<sub>2</sub>AlC and V<sub>2</sub>AlC) than for the solid-solution compositions. As the Nb:V ratio in (Nb<sub>2</sub>V<sub>2-y</sub>)AlC approached 1:1, peak attenuation and broadening for these vibrational modes were observed. This behavior is likely related to the random but uniform distribution of Nb and V atoms withing the MAX phase lattice, which would result in changes to Al-Nb-C and Al-V-C bond lengths. These differences in bond length may also give rise to interstitial defects, as Nb and V compete for crystallographic sites during MAX phase synthesis.

The most representative  $(Nb_{\nu}V_{2-\nu})$ AlC MAX phases (y = 0.00, 0.50, 1.00, 1.50, and2.00) were selected for TGA/DTA analysis (Figure S3a in Supporting Information). MAX phase oxidation is evidenced by both, the weight increase (associated with oxygen incorporation in the structure) and the simultaneous exothermic process happening at ~600 °C.<sup>37</sup> The TGA curves (Figure S3a in Supporting Information) show that the MAX phase mass remains stable up to ~500 °C, with a slight consistent decrease, probably due to the adsorbed water loss. A sharp weight increase follows until the curve reaches a maximum and forms a plateau, due to complete oxidation. The Nb-enriched compositions have lower maximum percentage mass variations compared to the V-enriched phases after reaching the plateau. Given that Nb<sub>2</sub>AlC is around 60% heavier than V<sub>2</sub>AlC, it is expected that the mass of V-enriched compositions will increase more than the Nb-enriched compositions, as more transition metal atoms are available for oxidation for the same mass of material. The maximum mass variations follow the respective atomic proportions, with a 61% variation difference from  $Nb_2AlC$  compared to  $V_2AlC$ , 37% from  $(Nb_{1.50}V_{0.50})AlC$ , 23% from  $(Nb_{1.00}V_{1.00})AlC$  and 10% from (Nb<sub>0.50</sub>V<sub>1.50</sub>)AlC. The single-transition metal MAX phases present the highest thermal oxidation temperature (T<sub>Ox</sub>), with V<sub>2</sub>AlC oxidizing at 729 °C and Nb<sub>2</sub>AlC oxidizing at 763 °C.

There is a gradual decrease in  $T_{Ox}$  towards the 1:1 ratio composition (**Figure S3b** in **Supporting Information**), which oxidized at 568 °C, indicating the reduction in the chemical and structural stability of the mixed phases as compared to the pure end compositions of the solid-solution (Nb<sub>y</sub>V<sub>2-y</sub>)AlC MAX phases (V<sub>2</sub>AlC and Nb<sub>2</sub>AlC). The thermal stability trend could be related to the discontinuities in the MAX phase crystalline structure with the insertion of the second transition metal, with its maximum destabilization at 1:1 V:Nb ratio, the farthest from the pure phases.

XRD patterns of powder multilayer (Nb<sub> $\nu$ </sub>V<sub>2- $\nu$ </sub>)CT<sub>x</sub> MXenes are shown in **Figure 2a**. The d-spacing, calculated from the position of (002) peak, varies between ~10 Å and ~12 Å, in agreement with the previous reports on V<sub>2</sub>CT<sub>x</sub> and Nb<sub>2</sub>CT<sub>x</sub>.<sup>25</sup> The shift in the (002) peak indicates that the Al atoms were removed, confirming successful MXene synthesis.<sup>38</sup> The dspacings of the MXenes are listed in Table 1. In contrast with the trend noted for the MAX phases, the MXene (002) d-spacing did not show consistent changes correlated with the niobium content. Rather, we observed higher (002) d-spacing values for MXenes with lower residual MAX phase content. The d-spacing of MXenes highly depends on the completenessof-etch during the MAX phase etching process and water content that can vary depending on the chemical composition. As the Nb:V ratio in  $(Nb_yV_{2-y})CT_x$  approached 1:1, the MXene XRD patterns revealed more complete etching is observed, suggesting that the solid-solution MAX phases are less chemically stable or resistant to etching, in agreement with the TGA/DTA analysis of the MAX phases (Figure S3 in Supporting Information). This analysis reveals a trend in solid-solution MAX chemical and oxidative stability, and likely applies to ternary or high-entropy MXenes. One potential explanation of this behavior is that at Nb:V ratios close to 1:1, the niobium and vanadium atoms compete for crystallographic sites during MAX phase synthesis, which can induce structural defects that improve the etching process. However, more extensive structural analysis is required to fully understand this mechanism.

**Table 1.** *d*-spacings of solid-solution  $(Nb_yV_{2-y})CT_x$  MXenes calculated from the position of (002) peak in corresponding XRD patterns.

y value	0.00	0.25	0.50	0.75	1.00	1.25	1.50	1.75	2.00
d-spacing, Å	9.75	9.56	11.78	11.84	12.00	11.84	12.07	12.27	10.42

 $(Nb_yV_{2-y})CT_x$  (y = 0, 0.25, 0.50, 0.75, 1.00, 1.25, 1.50, 1.75, and 2) samples were analysed using Raman spectroscopy to observe how changes in composition affect vibrational modes of MXenes (**Figure 2b**). In comparison to the Raman spectra of corresponding MAX

phases (**Figure S2** in **Supporting Information**), sharp peaks of the Al-related vibrations at 140-150 cm<sup>-1</sup> diminish, confirming etching success.<sup>36</sup>

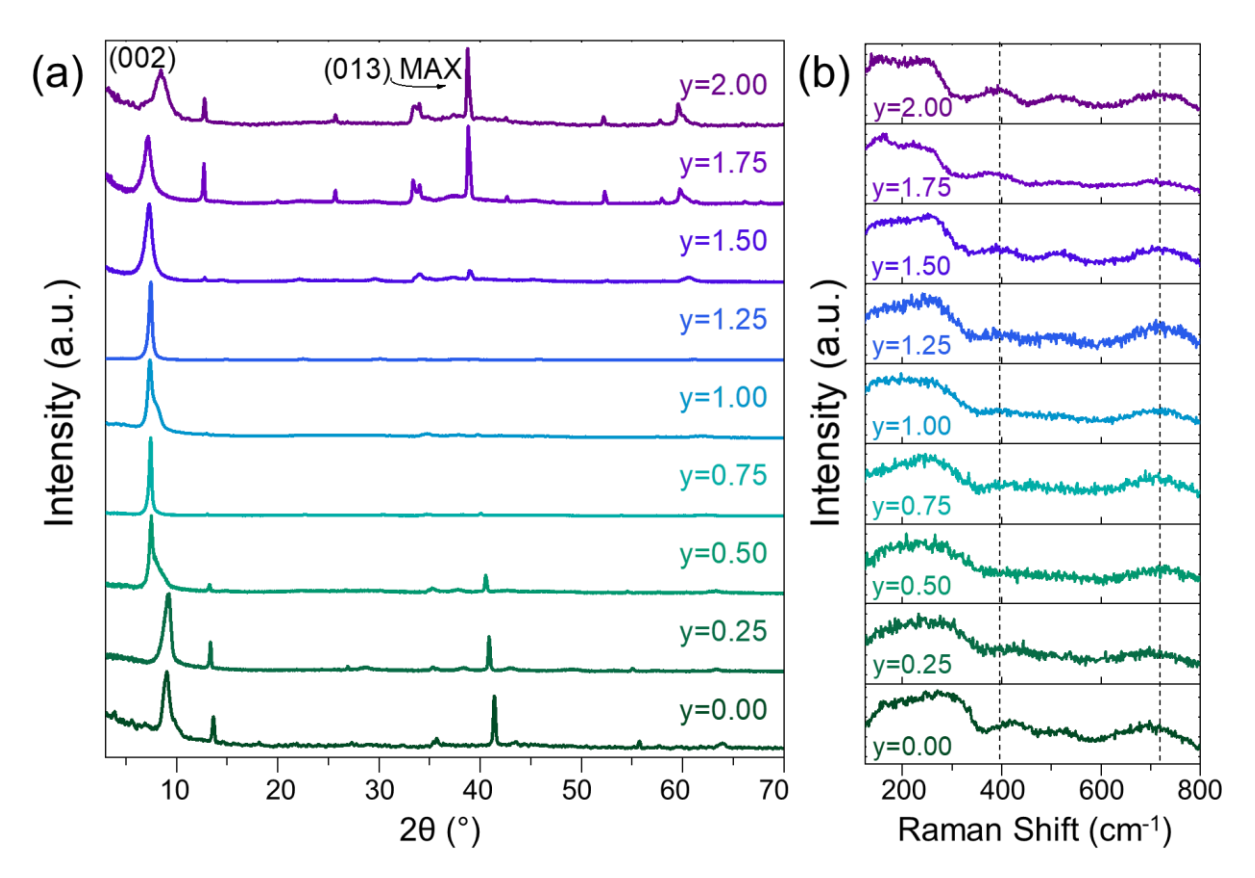


**Figure 2.** (a) X-ray diffraction patterns and (b) Raman spectra of  $(Nb_yV_{2-y})AlC$  (y= 0.00, 0.25, 0.50, 0.75, 1.00, 1.25, 1.50, 1.75, and 2.00) solid-solution MXenes. The (013) peak of the unetched parent MAX phase is indicated in the XRD patterns.

The Raman spectra of  $(Nb_yV_{2-y})CT_x$  MXenes (**Figure 2b**) show broader peaks compared to the corresponding MAX phases (**Figure S2** in **Supporting Information**), and peaks corresponding to the Al-related vibrations (277 cm<sup>-1</sup>, 421 cm<sup>-1</sup>, 530 cm<sup>-1</sup>, and 699 cm<sup>-1</sup>) diminish, signifying successful etching and MXene formation.<sup>36</sup> The E<sub>g</sub> and A<sub>1g</sub> vibrations giving signals in the lower frequency ranges (160-313 cm<sup>-1</sup>), while heavily dependent on the nature of M atom, include all atoms except the inactive middle carbon layer from  $M_2XT_x$  structure. In the pure  $V_2CT_x$  sample, the peaks are observed at 277 cm<sup>-1</sup> (broad peak ranging from 160 cm<sup>-1</sup> to 313 cm<sup>-1</sup>), 421 cm<sup>-1</sup>, 530 cm<sup>-1</sup>, and 699 cm<sup>-1</sup>, and the broadening of the peaks could suggest that there is more than one peak upon deconvolution. The spectrum matches the experimentally reported data and theoretical predictions, confirming that  $V_2CT_x$  was synthesized.<sup>39</sup> The broad peak around 160-313 cm<sup>-1</sup> is likely a combination of E<sub>g</sub> and A<sub>1g</sub> modes corresponding to in-plane vibration and out-of-plane vibration of transition metal atoms,

and it changes from pure  $V_2C$  spectra with the addition of Nb. The low frequency  $A_{1g}$  mode shifts to lower wavenumber with the increase of transition metal mass (V < Nb), which can be observed with  $A_{1g}$  peak shifting from 277 cm<sup>-1</sup> in  $V_2CT_x$  sample to 244 cm<sup>-1</sup> in  $Nb_2CT_x$  sample.<sup>25</sup> All the other modes depend on terminal groups and the lack of clear spectral trends proves that they are heterogeneous/randomly distributed.<sup>39</sup>

While there are no theoretical predictions for Raman spectra of  $Nb_2CT_x$  MXene, the spectra match the results observed before. The peak in the Raman spectrum of  $Nb_2CT_x$  MXene in the 700 cm<sup>-1</sup> region has about 50% lower intensity than the corresponding peak in the Raman spectrum of  $V_2CT_x$  sample. Additionally, this peak shifts to higher wavenumbers - in the direction opposite to the shift observed for peaks below 600 cm<sup>-1</sup>. The changes in this peak positions have been attributed to differences in surface terminations. The first broad peak in the Raman spectra of MXenes enriched with Nb  $\{(Nb_{1.75} \ V_{0.25})CT_x \ and \ Nb_2CT_x\}$  is split with the maxima at 156 and 244 cm<sup>-1</sup>, corresponding to  $E_g$  and  $A_{1g}$  modes (in-plane vibration and out-of-plane vibration of Nb atoms). The peaks in the 400-600 cm<sup>-1</sup> range assigned to MXene surface terminations are present in  $Nb_2CT_x$  and  $V_2CT_x$  samples, and diminish in intensity as MXene compositions get closer to Nb:V ratio of 1:1  $\{(Nb_{0.50}V_{1.50})CT_x - (Nb_{1.00}V_{1.00})CT_x\}$ . It was shown before that the significant broadening of the peaks is a result of distortions of nearby unit cells caused by different M-elements, since Raman vibrations in materials represent the vibrations of a unit cell.

The  $(Nb_yV_{2-y})CT_x$  MXenes were transformed into oxides by a reaction with  $H_2O_2$  followed by hydrothermal treatment. The transformation process can be tracked by the change in color of the MXene at each step (**Figure 3**). These colors are indicative of the oxidation state of the transition metals as the MXenes are oxidized. After the initial dissolution of the MXene in water in the presence of  $H_2O_2$ , the V-enriched compositions display a variety of colors while the Nb-enriched compositions remain black (**Figure 3a**). The colors of these intermediate solutions have not been documented in literature and the physical and chemical characteristics of these intermediates are the subject of future study. After the hydrothermal treatment (**Figure 3b**), the color of the mixtures changed substantially and were similar to the final oxide products (**Figure 3c**) obtained after washing and drying. Vanadium system is well known for the established relationship between the solution color and oxidation state of vanadium; niobium shares a similar, but not as pronounced feature. The color change after hydrothermal treatment indicates the further transformation of the dissolved MXene. The dark green color of the Venriched compositions is indicative of mixed  $V^{5+}/V^{4+}$  oxidation state, while the white color of the Nb-enriched compositions indicates  $Nb^{5+}$  oxidation state. As the composition moves

towards the 1:1 Nb:V ratio, the color becomes browner and may be indicative of the mixture of V<sup>5+</sup> and Nb<sup>5+</sup>. Further work needs to be done to understand the character of the intermediate mixture and how the chemical change is facilitated during hydrothermal treatment.

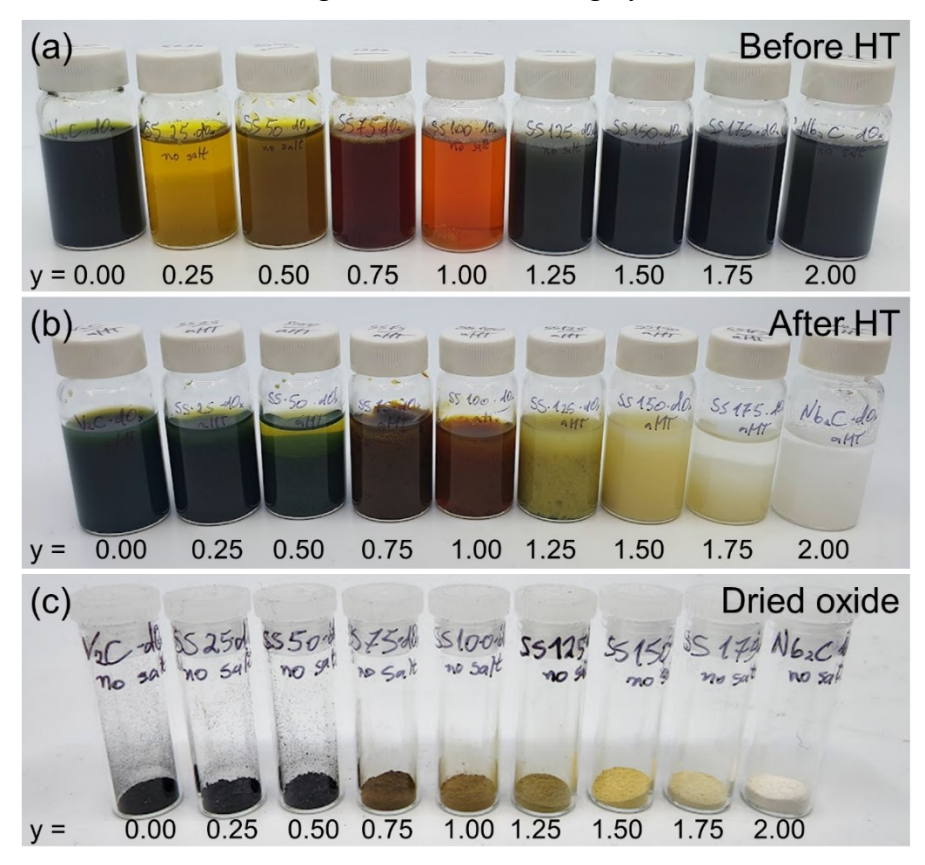


**Figure 3.** Evolution of the sample appearance during multi-step synthesis process shown in the digital photographs of the SS-MXene-dOX during different steps of the transformation into oxides: (a) SS-MXene-dOX after dissolution in H<sub>2</sub>O<sub>2</sub> and stirring for 5 h, (b) SS-MXene-dOX after hydrothermal treatment at 140 °C for 24h, and (c) SS-MXene-dOX after washing and drying at 105 °C in air for 24h.

The XRD patterns of SS-MXene-dOX (**Figure 4a**) reveal a trend corresponding to the composition on the oxide products. The XRD patterns obtained for  $V_2CT_x$ -dOX are typical for the bilayered vanadium oxide (BVO) with the *d*-spacing of 12.7 Å, which is slightly larger than the values reported for the BVO stabilized with water only<sup>5</sup> and could be attributed to the increased interlayer water content. These BVO peaks are also observed in the XRD patterns of Nb-containing compositions up to  $(Nb_{1.25}V_{0.75})CT_x$ -dOX, at around 7° and 26° 2 $\theta$ , with the decrease of relative intensities as the niobium concentration increases. For the Nb-enriched phases, XRD patterns show broad peaks, corresponding to nanostructured amorphous Nb<sub>2</sub>O<sub>5</sub> (nANO). The nANO peaks remain in the XRD patterns as the vanadium concentration increases, up to the  $(Nb_{0.75}V_{1.25})CT_x$ -dOX. In case of the  $(Nb_yV_{2-y})CT_x$ -dOX compositions with y = 0.75, 1.00, 1.25, there is clear evidence of a two-phase system of BVO and nANO, with a

peak shift of the (002) BVO peak to the larger  $2\theta$  values (smaller *d*-spacing) as Nb concentration increases. This peak shift, and subsequent reduction in *d*-spacing, may be related to the intercalation of niobium atoms into the BVO interlayer region, similar to the change in *d*-spacing observed with intercalating larger alkali ions.<sup>11</sup>

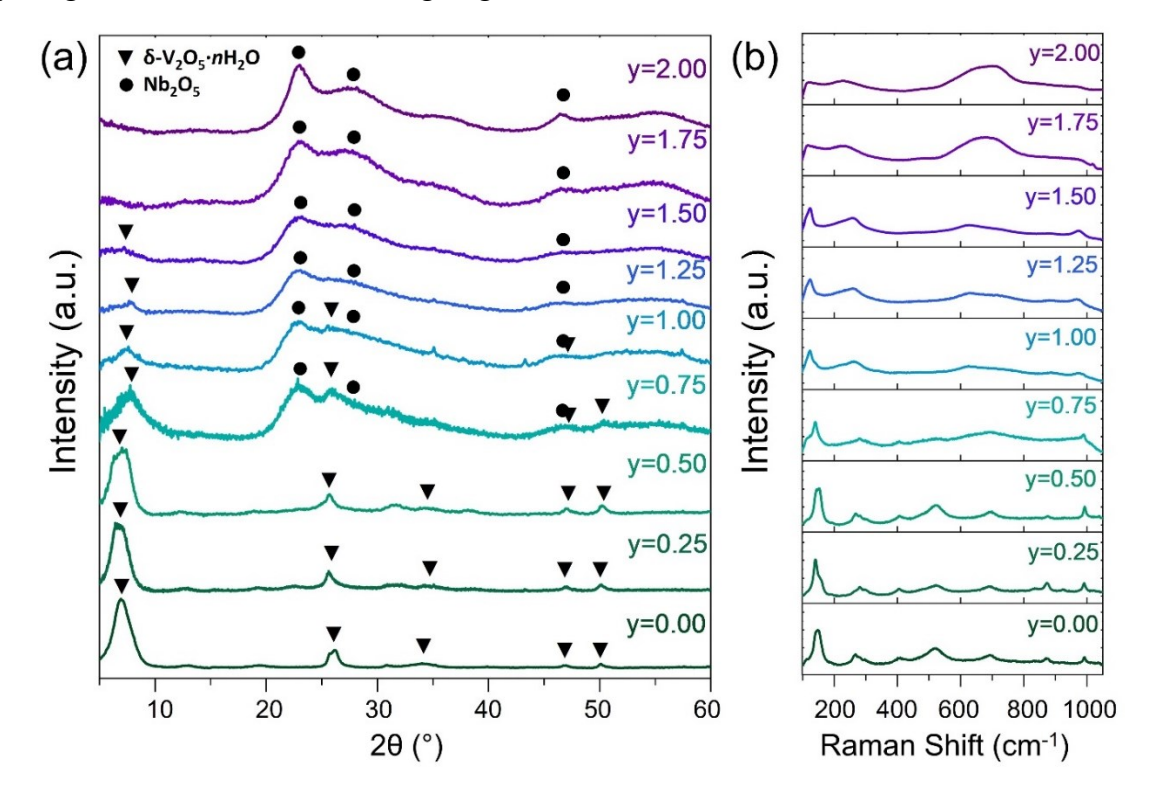


**Figure 4.** (a) X-ray diffraction patterns and (b) Raman spectra of oxides derived from  $(Nb_yV_{2-y})CT_x$  MXenes.

Raman spectra of SS-MXene-dOX (**Figure 4b**) show a similar trend to the XRD patterns. The vanadium-enriched phases show characteristic features of BVO, with peak broadening occurring as the niobium content increases. Particularly, the following peaks correspond to the specific bonds in the BVO structure: 149 cm<sup>-1</sup> - the skeletal bending mode indicative of long range ordering; 265 cm<sup>-1</sup> - the antisymmetric bending mode of in-plane O-V-O bonds; 403 cm<sup>-1</sup> - the symmetric bending mode of in-plane V-O-V bonds; 521 cm<sup>-1</sup> - the antisymmetric bending mode of terminal V-O bonds; 695 cm<sup>-1</sup> - the antisymmetric stretching mode of V-O bonds involving bridging oxygens; 876 cm<sup>-1</sup> - the antisymmetric stretching mode of out-plane V-O-V bonds; and 992 cm<sup>-1</sup> - the symmetric stretching mode of terminal V=O bonds. Interestingly, the peaks at  $\sim$ 149, 265, and 992 cm<sup>-1</sup> are preserved up to y = 1.50 {(Nb<sub>1.50</sub>V<sub>0.5</sub>)CT<sub>x</sub>}, indicating that BVO forms even for the niobium-enriched compositions. Likewise, the Raman spectrum of Nb<sub>2</sub>CT<sub>x</sub>-dOX contains features characteristic of amorphous Nb<sub>2</sub>O<sub>5</sub>: peak at 227 cm<sup>-1</sup> corresponds to the bending mode for Nb-O-Nb bonds; peak at 680 cm<sup>-1</sup>

 $^{1}$  is assigned to the symmetric stretching mode of NbO<sub>6</sub>, NbO<sub>7</sub>, and NbO<sub>8</sub> polyhedra; and peak at 963 cm<sup>-1</sup> correlates with the symmetric stretching mode of Nb=O bonds.  $^{18}$  The spectra of the niobium-enriched (Nb<sub>1.75</sub>V<sub>0.25</sub>)CT<sub>x</sub>-dOX and Nb<sub>2.00</sub>CT<sub>x</sub>-dOX are similar to that of nANO.  $^{18}$  The features of nANO can also be seen in the Raman spectra corresponding to compositions with y = 0.75 - 1.50, indicating the formation of a two-phase BVO/nANO system. Because BVO peaks at 403, 521, 876, and 992 cm<sup>-1</sup> disappear at these intermediary compositions, while the nANO peak at 680 cm<sup>-1</sup> is getting suppressed, this new spectral behavior indicates the formation of some new structure that does not appear in the XRD patterns. These observed interactions may be evidence of a heterointerface forming between the BVO and nANO particles for y = 0.75 - 1.50. This heterointerface may affect the electrochemical behavior of the two-phase system due to a synergistic effect of the two oxides.  $^{1, 43}$ 

SEM images of V<sub>2</sub>CT<sub>x</sub>-dOX, Nb<sub>2</sub>CT<sub>x</sub>-dOX, and (Nb<sub>1.00</sub>V<sub>1.00</sub>)CT<sub>x</sub>-dOX (**Figure 5**) reveal additional information about the structural trends observed in the XRD patterns. The SEM images of V<sub>2</sub>CT<sub>x</sub>-dOX (**Figure 5a,b**) show crumpled sheet-like particles of BVO composed by intergrown nanoribbons with ~200 nm widths. Previous works related to BVO synthesis using orthorhombic vanadium oxide as a precursor material reported analogous nanoribbon morphology. Similar morphology was also reported for V<sub>2</sub>CT<sub>x</sub>-derived lithium-preintercalated bilayered vanadium oxide, where nanobelt sections fused and formed 2D nanoflake-like particles assembled into a porous film. Therefore, our results support the notion that by using MXenes as precursors for BVO synthesis, 2D morphologies can be stabilized unique to previous BVO synthesis routes producing 1D particles such as nanobelts. By including alkali or alkali earth ions, nanoflake morphologies can be modified into flower-like particles with high surface areas.

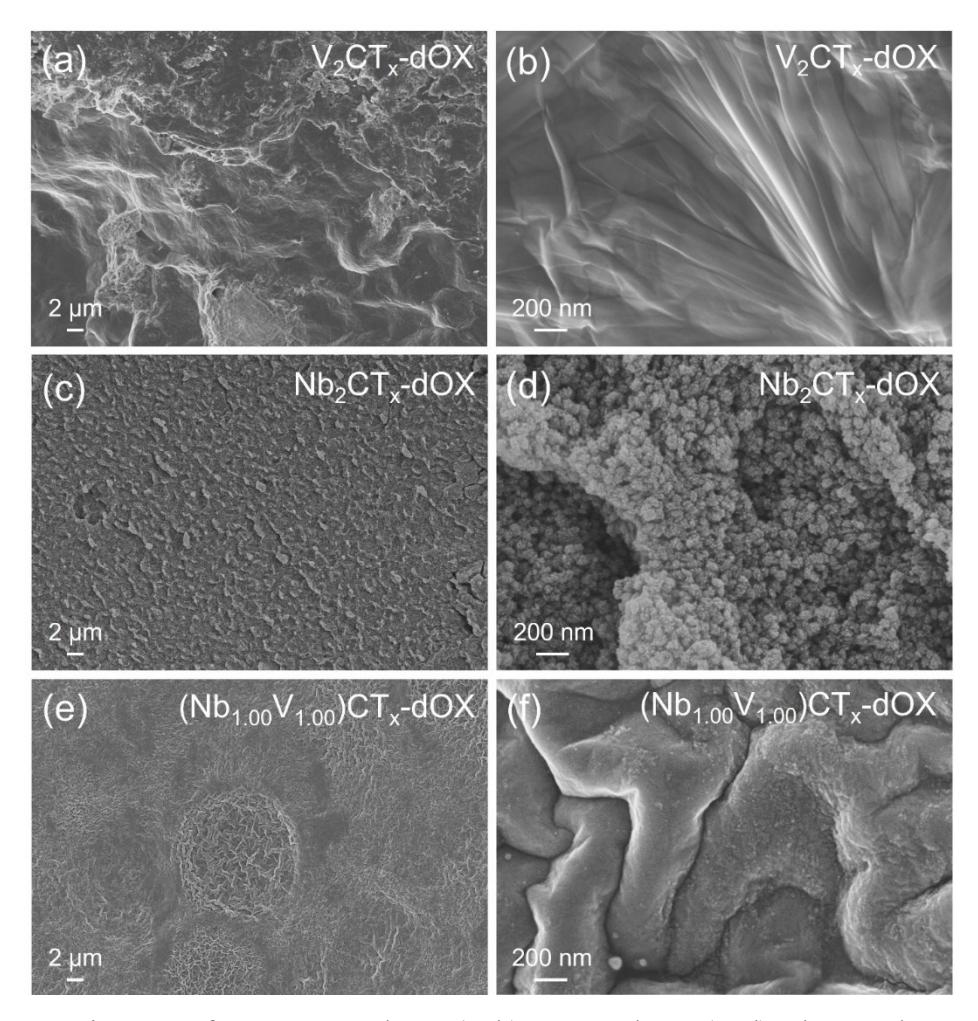


**Figure 5.** SEM images of SS-MXene-dOX: (a, b)  $V_2CT_x$ -dOX, (c, d)  $Nb_2CT_x$ -dOX, and (e, f)  $(Nb_{1.00}V_{1.00})CT_x$ -dOX. (a, c, e) Low and (b, d, f) high magnification images are shown.

The SEM images of Nb<sub>2</sub>CT<sub>x</sub>-dOX (**Figure 5c,d**) show the formation of a porous network of spherical nanoparticles that range from 4 nm to 30 nm in diameter and cluster into agglomerates typically with a diameter between 75 and 200 nm. Similar morphology has been reported for other nanostructured amorphous Nb<sub>2</sub>O<sub>5</sub>.<sup>15</sup> The SEM images of (Nb<sub>1.00</sub>V<sub>1.00</sub>)CT<sub>x</sub>-dOX powder (**Figure 5e,f**) show particles with both BVO and nANO features. At low magnification (**Figure 5e**), the sheets of BVO are clearly visible with two distinct regions: patches of crumpled sheets and flat sheets surrounding those patches. SEM images at higher magnifications (**Figure 5f**) show spherical nanoparticles, consistent with Nb<sub>2</sub>CT<sub>x</sub>-dOX, <sup>15</sup> grown on the surface of the BVO sheets. The presence of the two distinctly different morphologies agrees with the XRD pattern of this material showing the presence of both BVO and nANO phases.

**Figure 6** shows the electrochemical performance of (Nb<sub>y</sub>V<sub>2-y</sub>)CT<sub>x</sub>-dOX electrodes in non-aqueous Li-ion cells. The shapes of CV curves exhibited by the cells containing V<sub>2</sub>CT<sub>x</sub>-dOX (**Figure 6a**) and Nb<sub>2</sub>CT<sub>x</sub>-dOX (**Figure 6i**) electrodes agree with the literature data for BVO<sup>45, 46</sup> and nANO<sup>15</sup>, respectively. The CV curve of the V<sub>2</sub>CT<sub>x</sub>-dOX shows a reversible peak corresponding to Li<sup>+</sup> ion intercalation at ~2.70 V and extraction at ~3.25 V, as typical for the BVO phases<sup>46</sup>. The low capacity of ~110 mAh·g<sup>-1</sup> can be attributed to high interlayer water content in the δ-V<sub>2</sub>O<sub>5</sub>·nH<sub>2</sub>O structure which agrees with the 12.7 Å *d*-spacing.<sup>34</sup> Furthermore, the lack of pre-intercalated ions to stabilize BVO can result in structural collapse during cycling, decreasing the material performance.<sup>8, 11</sup> nANO, on the other hand, exhibits pseudocapacitive charge storage behavior at anodic potentials < 2.50 V. The CV curve of the Nb<sub>2</sub>CT<sub>x</sub>-dOX presents a high capacity above 200 mAh·g<sup>-1</sup> within the potential window of 1.00 – 4.00 V with good initial cyclability (**Figure 6i**).

The electrochemical behavior of vanadium-rich (Nb<sub>y</sub>V<sub>2-y</sub>)CT<sub>x</sub>-dOX showed features never exhibited by BVO electrodes. The CV curve of the Li-ion cell containing (Nb<sub>0.25</sub>V<sub>1.75</sub>)CT<sub>x</sub>-dOX electrode (**Figure 6b**) exhibits discharge peaks at 1.58 V, 1.94 V, 2.41 V, and 2.84 V with corresponding charge peaks at 1.78 V, 2.17 V, 2.71 V, and 3.35 V, respectively. The two higher potential peaks are characteristic of Li<sup>+</sup> ions intercalation into BVO structure, while the two lower potential peaks are newly observed features.<sup>47</sup> These new features may be a result of a niobium doping, either in the BVO lattice or within the BVO interlayer region. (Nb<sub>0.25</sub>V<sub>1.75</sub>)CT<sub>x</sub>-dOX exhibited an initial capacity of 296.8 mAh·g<sup>-1</sup>, which is significantly higher than that of V<sub>2</sub>CT<sub>x</sub>-dOX. Additionally, the initial stability of the CV curves is fairly good, showing little change in shape over 5 cycles. These improvements over

the  $V_2CT_x$ -dOX material may stem from the aforementioned niobium doping, but further work must be done to determine structural aspects of the (Nb<sub>0.25</sub>V<sub>1.75</sub>)CT<sub>x</sub>-dOX phase.

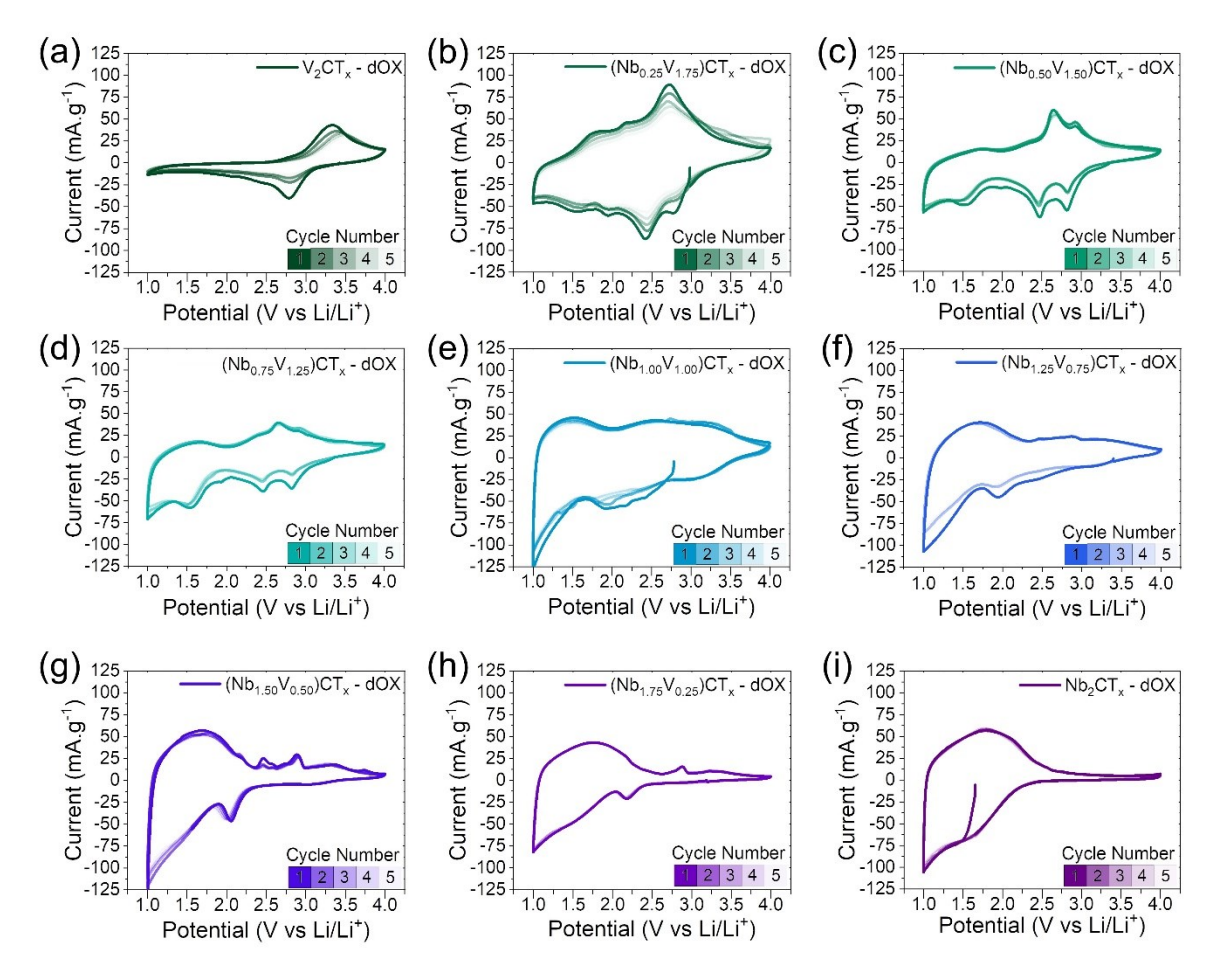


**Figure 6.** Cyclic voltammograms of the first 5 cycles exhibited by Li-ion cells containing (a)  $V_2CT_x$ -dOX, (b)  $(Nb_{0.25}V_{1.75})CT_x$ -dOX, (c)  $(Nb_{0.50}V_{1.50})CT_x$ -dOX, (d)  $(Nb_{0.75}V_{1.25})CT_x$ -dOX, (e)  $(Nb_{1.00}V_{1.00})CT_x$ -dOX, (f)  $(Nb_{1.25}V_{0.75})CT_x$ -dOX, (g)  $(Nb_{1.50}V_{0.50})CT_x$ -dOX, (h)  $(Nb_{1.75}V_{0.25})CT_x$ -dOX, and (i)  $Nb_2CT_x$ -dOX. All cells were cycled at 0.1 mV·s<sup>-1</sup>.

As the niobium content increases, the CV profiles exhibited by Li-ion cells containing (Nb<sub>y</sub>V<sub>1-y</sub>)CT<sub>x</sub>-dOX electrodes begin to change: the large area observed in the CV curve of (Nb<sub>0.25</sub>V<sub>1.75</sub>)CT<sub>x</sub>-dOX electrode shrinks, and the redox peaks resemble the profile for the BVO more closely, while the rectangular region at lower potentials, typical for Nb<sub>2</sub>O<sub>5</sub>, gradually develops. CV curves of (Nb<sub>0.50</sub>V<sub>1.50</sub>)CT<sub>x</sub>-dOX (**Figure 6c**) and (Nb<sub>0.75</sub>V<sub>1.25</sub>)CT<sub>x</sub>-dOX (**Figure 6d**) electrodes feature Li<sup>+</sup> ion insertion/extraction peaks at 2.47 and 2.82 V on discharge and at 2.64 and 2.92 V on charge which correspond to the behavior of ion-preintercalated BVO.<sup>11</sup> The area below 2.00 V is attributed to the pseudocapacitive behavior of nANO cycled in non-aqueous Li-ion systems.<sup>15</sup> These cells exhibited initial capacities of 171.2 mAh·g<sup>-1</sup> and 160.8 mAh·g<sup>-1</sup>, respectively, with good 5-cycle stability. Interestingly, while the CV curves of both

(Nb<sub>0.5</sub>V<sub>1.5</sub>)CT<sub>x</sub>-dOX and (Nb<sub>0.75</sub>V<sub>1.25</sub>)CT<sub>x</sub>-dOX electrodes clearly show features corresponding to nANO, the nANO peaks are clearly seen in the XRD pattern of the (Nb<sub>0.75</sub>V<sub>1.25</sub>)CT<sub>x</sub>-dOX, but absent in the XRD pattern of (Nb<sub>0.50</sub>V<sub>1.50</sub>)CT<sub>x</sub>-dOX (**Figure 4a**). It is possible that for the solid-solution composition with y = 0.5, the amount of the forming nANO particles is not high enough to appear in XRD patterns. Electrochemical characterization, though, shows their presence appearing as a more sensitive method to detect amorphous material component in nanocomposites structure.

The CV curve of the cell containing (Nb<sub>1.00</sub>V<sub>1.00</sub>)CT<sub>x</sub>-dOX electrode (**Figure 6e**) shows a shape with no peaks corresponding to the redox activity of BVO. Instead, the rectangular CV curve shape pertains to predominantly pseudocapacitor-like behavior. The cell containing (Nb<sub>1.00</sub>V<sub>1.00</sub>)CT<sub>x</sub>-dOX electrode exhibited an initial capacity of 297.8 mAh·g<sup>-1</sup> with good initial stability. The large rectangular area below 2.0 V and the corresponding capacity are likely attributed to the increased content of nANO particles, as evidenced by the XRD pattern (**Figure 4a**) and SEM images (**Figure 5e, f**) of (Nb<sub>1.00</sub>V<sub>1.00</sub>)CT<sub>x</sub>-dOX. The difference in CV curve shapes between this cell and the cells containing V-enriched derived oxides may indicate a difference in where niobium resides in the structure. While nANO is present in both cases, there is likely a greater amount of niobium doping in the V-enriched phases, while (Nb<sub>1.00</sub>V<sub>1.00</sub>)CT<sub>x</sub>-dOX may predominantly contain Nb in the form of nANO and very little Nb doping in the BVO. Due to the formation of a tight heterointerface between the BVO and nANO phases in (Nb<sub>1.00</sub>V<sub>1.00</sub>)CT<sub>x</sub>-dOX, the two phases can interact synergistically when (Nb<sub>1.00</sub>V<sub>1.00</sub>)CT<sub>x</sub>-dOX is used as an electrode material in Li-ion cells, and therefore this material was selected for further electrochemical characterization in this work.

The CV curves of the cells containing (Nb<sub>1.25</sub>V<sub>0.75</sub>)CT<sub>x</sub>-dOX (**Figure 6f**), (Nb<sub>1.50</sub>V<sub>0.50</sub>)CT<sub>x</sub>-dOX (**Figure 6g**), and (Nb<sub>1.75</sub>V<sub>0.25</sub>)CT<sub>x</sub>-dOX (**Figure 6h**) electrodes show shapes dominated by a rectangular area corresponding to nANO charge storage behavior, while some activity characteristic of BVO contribution is still evident. These curves feature shapes below 2.00 V that are characteristic of nANO.<sup>15</sup> The cells containing (Nb<sub>1.25</sub>V<sub>0.75</sub>)CT<sub>x</sub>-dOX, (Nb<sub>1.50</sub>V<sub>0.50</sub>)CT<sub>x</sub>-dOX, and (Nb<sub>1.75</sub>V<sub>0.25</sub>)CT<sub>x</sub>-dOX electrodes exhibited initial capacities of 198.8 mAh·g<sup>-1</sup>, 224.8 mAh·g<sup>-1</sup>, and 157.2 mAh·g<sup>-1</sup>, respectively, with excellent 5-cycle stability that improved with increasing Nb content. The peak on Li<sup>+</sup> ion insertion that was observed in the CV curve of (Nb<sub>1.00</sub>V<sub>1.00</sub>)CT<sub>x</sub>-dOX at 1.95 V is now more prominent, stable, and may have a redox pair on extraction at 2.90 V. The position of this reversible peak moves to higher potentials as the niobium content increases; it appears at 2.05 V in the discharge part of the CV curve of (Nb<sub>1.50</sub>V<sub>0.50</sub>)CT<sub>x</sub>-dOX electrode and at 2.20 V in the discharge part of the

CV curve of  $(Nb_{1.75}V_{0.25})CT_x$ -dOX electrode. The CV curve of  $(Nb_{1.50}V_{0.50})CT_x$ -dOX electrode also features several minor peaks on extraction at 2.10 V, 2.45 V, and 2.55 V. These peaks could be related to the vanadium doping into the  $Nb_2O_5$  structure resulting in redox activity at potentials above 2.0 V. However, additional study is needed to fully understand the structure and electrochemical behaviour of the  $(Nb_yV_{2-y})CT_x$ -derived oxides enriched in Nb.

Because of its composition, with equiatomic Nb and V,  $(Nb_{1.00}V_{1.00})CT_x$ -dOX was selected for extended electrochemical cycling to better understand the potential advantages of using SS MXenes as precursors for oxides synthesis. The Li-ion cells containing (Nb<sub>1.00</sub>V<sub>1.00</sub>)CT<sub>x</sub>-dOX electrode were compared with the cells containing an electrode prepared by physically mixing V<sub>2</sub>CT<sub>x</sub>-dOX and Nb<sub>2</sub>CT<sub>x</sub>-dOX with a V:Nb molar ratio of 1:1 (V<sub>2</sub>CT<sub>x</sub>dOX/Nb<sub>2</sub>CT<sub>x</sub>-dOX-1:1). The CV curves of the cells containing (Nb<sub>1.00</sub>V<sub>1.00</sub>)CT<sub>x</sub>-dOX (**Figure** 7a) and  $V_2CT_x$ -dOX/Nb<sub>2</sub>CT<sub>x</sub>-dOX-1:1 (Figure 7b) electrodes show similarities in the overall shape. The CV curves of both electrodes exhibit two rectangular areas with activity above 2.0 V attributed to the BVO and activity below 2.0 V ascribed to nANO components. At the same time, while the CV curve of the (Nb<sub>1.00</sub>V<sub>1.00</sub>)CT<sub>x</sub>-dOX electrode does not feature any definitive redox peaks over 5 cycles, the V<sub>2</sub>CT<sub>x</sub>-dOX/Nb<sub>2</sub>CT<sub>x</sub>-dOX-1:1 CV shows some Li<sup>+</sup> intercalation/extraction peaks above 2.0 V that quickly degrade. The insertion peaks at 2.38 V and 2.79 V and extraction peaks at 2.74 V and 3.01 V in V<sub>2</sub>CT<sub>x</sub>-dOX/Nb<sub>2</sub>CT<sub>x</sub>-dOX-1:1 CV are characteristic of BVO, and the rectangular area below 2.00 V is representative of nANO. 15, 46 The  $V_2CT_x$ -dOX/Nb<sub>2</sub>CT<sub>x</sub>-dOX-1:1 electrode exhibited an initial capacity of 308.0 mAh·g<sup>-1</sup>, which was higher than the initial capacity of  $(Nb_{1.00}V_{1.00})CT_x$ -dOX electrode (297.8 mAh·g<sup>-1</sup>). The higher initial capacity of the physical mixture electrode could be due to better penetration of electrolyte into redox-active BVO.

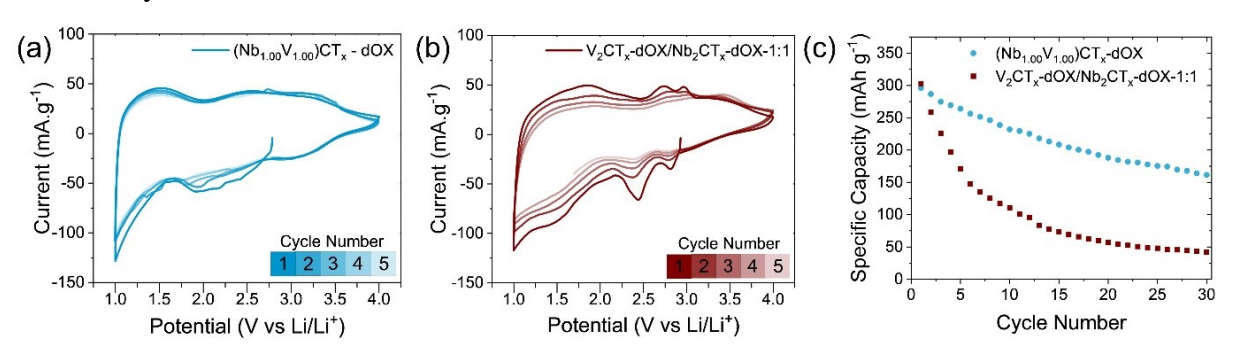


**Figure 7.** Comparison of the electrochemical behaviours of  $(Nb_{1.00}V_{1.00})CT_x$ -dOX and  $V_2CT_x$ -dOX/Nb<sub>2</sub>CT<sub>x</sub>-dOX-1:1 in Li-ion cells. (a,b) Cyclic voltammograms of the cells containing (a)  $(Nb_{1.00}V_{1.00})CT_x$ -dOX and (b)  $V_2CT_x$ -dOX/Nb<sub>2</sub>CT<sub>x</sub>-dOX-1:1, and (c) specific capacity vs. cycle number for  $(Nb_{1.00}V_{1.00})CT_x$ -dOX and  $V_2CT_x$ -dOX/Nb<sub>2</sub>CT<sub>x</sub>-dOX-1:1 electrodes.

However, the (Nb<sub>1.00</sub>V<sub>1.00</sub>)CT<sub>x</sub>-dOX electrode demonstrated better electrochemical stability compared to the physical mixture, as revealed by galvanostatic cycling of (Nb<sub>1.00</sub>V<sub>1.00</sub>)CT<sub>x</sub>-dOX and V<sub>2</sub>CT<sub>x</sub>-dOX/Nb<sub>2</sub>CT<sub>x</sub>-dOX-1:1 electrodes for 30 cycles (**Figure 7c**). The (Nb<sub>1.00</sub>V<sub>1.00</sub>)CT<sub>x</sub>-dOX cycling data showed a capacity retention of 38% while the V<sub>2</sub>CT<sub>x</sub>-dOX/Nb<sub>2</sub>CT<sub>x</sub>-dOX-1:1 data showed only 12% capacity retention after 30 cycles. The improved stability of the (Nb<sub>1.00</sub>V<sub>1.00</sub>)CT<sub>x</sub>-derived oxide electrode is attributed to the formation of a tight heterointerface between the BVO and nANO components. Similar heterointerface stabilizing behaviors have been reported for nanocomposite electrodes. While strategies to further improve electrochemical stability need to be developed, the use of solid-solution MXenes as precursors for oxide electrodes synthesis shows opportunities to achieve doping and heterointerface formation.

## 4. Conclusions

We have synthesized a range of  $(Nb_{\nu}V_{2-\nu})$ AlC MAX phase solid-solution compositions (y = 0.00, 0.25, 0.50, 0.75, 1.00, 1.25, 1.50, 1.75, and 2.00), etched them to form  $(Nb_{\nu}V_{2-\nu})CT_{x}$ solid-solution MXenes, and converted these MXenes into oxides. We found that etching the mixed MAX phase composition was more rapid than the end members of this family. The solidsolution MXene-to-oxide transformation was achieved through a two-step process of dissolution initiated by hydrogen peroxide followed by hydrothermal treatment. Following this synthesis route with  $V_2CT_x$  MXene precursor, we obtained  $\delta$ - $V_2O_5$ · $nH_2O$  (BVO) with a crumpled sheet morphology, while for Nb<sub>2</sub>CT<sub>x</sub> precursor, amorphous Nb<sub>2</sub>O<sub>5</sub> (nANO) nanoparticles with  $\sim 20$  nm diameter were synthesized. For the mixed compositions (y = 0.25, 0.50, 0.75, 1.00, 1.25, 1.50, 1.75) our synthesis route led to the formation of nanocomposites containing both BVO and nANO, evidenced by XRD, SEM and electrochemical cycling analysis. The features in the CV curves of the non-aqueous Li-ion cells containing the (Nb<sub>0.25</sub>V<sub>1.75</sub>)CT<sub>x</sub>-dOX and (Nb<sub>1.75</sub>V<sub>0.25</sub>)CT<sub>x</sub>-dOX electrodes suggest the possibility of Nb doping into V-sites in BVO and V doping in Nb sites in nANO, respectively, calling for a detailed investigation of structure and electrochemistry of these materials. The electrochemical behavior of (Nb<sub>1.00</sub>V<sub>1.00</sub>)CT<sub>x</sub>-dOX appeared to be the most exciting due to the largest initial capacity of ~300 mAh·g<sup>-1</sup> with a minimal capacity decay in the first five cycles. A comparison of capacity retention shown by  $(Nb_{1.00}V_{1.00})CT_x$ -dOX and an electrode prepared by physically mixing V<sub>2</sub>CT<sub>x</sub>-dOX and Nb<sub>2</sub>CT<sub>x</sub>-dOX in 1:1 molar V:Nb ratio over 30 cycles revealed the superior electrochemical stability of the solid-solution MXene derived electrode. The improved capacity retention was attributed to a tight heterointerface formed between the BVO and nANO

particles in  $(Nb_{1.00}V_{1.00})CT_x$ -dOX, revealed by the SEM analysis, that cannot be achieved by simple physical mixing.

As shown through this study, synthesis of complex oxides tremendously benefits from the use of solid-solution MXenes as precursors. Incorporation of multiple transition metals in oxide structures could enhance functionality, and previously reported MXene-derived oxides can be augmented for ferroelectric<sup>3</sup> and photocatalytic<sup>51</sup> applications. Solid-solution MXenes are not limited to two transition metals, and the expansion of the composition to include three or more metals can lead to truly unique and novel derivatives that cannot be achieved using traditional synthetic techniques.

**Supporting Information.** XRD, Raman spectroscopy and DTA/TGA characterization of the  $(Nb_{\nu}V_{2-\nu})AlC$  MAX phases.

## Acknowledgements

We thank the National Science Foundation for providing funding for this research under Grant No. DMR-1752623. MXene materials development was supported by Murata Manufacturing. M.A.A. was supported through |MESC+ Erasmus Mundus program by the European Union. XRD and SEM analysis were conducted using instruments in the Materials Characterization Core (MCC) at Drexel University.

#### 5. References

- (1) Pomerantseva, E.; Bonaccorso, F.; Feng, X.; Cui, Y.; Gogotsi, Y. Energy storage: The future enabled by nanomaterials. *Science* **2019**, 366, eaan8285.
- (2) Baig, N.; Kammakakam, I.; Falath, W. Nanomaterials: a review of synthesis methods, properties, recent progress, and challenges. *Materials Advances* **2021**, *2* (6), 1821-1871.
- (3) Tu, S.; Ming, F.; Zhang, J.; Zhang, X.; Alshareef, H. N. MXene-Derived Ferroelectric Crystals. *Advanced Materials* **2019**, *31* (14), 1806860.
- (4) Ridley, P.; Gallano, C.; Andris, R.; Shuck, C. E.; Gogotsi, Y.; Pomerantseva, E. MXene-Derived Bilayered Vanadium Oxides with Enhanced Stability in Li-Ion Batteries. *ACS Applied Energy Materials* **2020**, *3* (11), 10892-10901.
- (5) Clites, M.; W. Byles, B.; Pomerantseva, E. Bilayered vanadium oxide as the host material for reversible beyond lithium ion intercalation. *Advanced Materials Letters* **2017**, *8* (6), 679-688.
- (6) Petkov, V.; Trikalitis, P. N.; Bozin, E. S.; Billinge, S. J. L.; Vogt, T.; Kanatzidis, M. G. Structure of V<sub>2</sub>O<sub>5</sub>·nH<sub>2</sub>O Xerogel Solved by the Atomic Pair Distribution Function Technique. *Journal of the American Chemical Society* **2002**, *124* (34), 10157-10162.
- (7) Xu, X.; Xiong, F.; Meng, J.; Wang, X.; Niu, C.; An, Q.; Mai, L. Vanadium-Based Nanomaterials: A Promising Family for Emerging Metal-Ion Batteries. *Advanced Functional Materials* **2020**, *30* (10), 1904398.
- (8) Pomerantseva, E. Chemical Preintercalation Synthesis of Versatile Electrode Materials for Electrochemical Energy Storage. *Accounts of Chemical Research* **2023**, *56* (1), 13-24.
- (9) Liu, Z.; Sun, H.; Qin, L.; Cao, X.; Zhou, J.; Pan, A.; Fang, G.; Liang, S. Interlayer Doping in Layered Vanadium Oxides for Low-cost Energy Storage: Sodium-ion Batteries and Aqueous Zinc-ion Batteries. *ChemNanoMat* **2020**, *6* (11), 1553-1566.
- (10) Coustier, F.; Passerini, S.; Smyrl, W. H. Dip-coated silver-doped V<sub>2</sub>O<sub>5</sub> xerogels as host materials for lithium intercalation. *Solid State Ionics* **1997**, *100* (3), 247-258.
- (11) Clites, M.; Pomerantseva, E. Bilayered vanadium oxides by chemical pre-intercalation of alkali and alkali-earth ions as battery electrodes. *Energy Storage Materials* **2018**, *11*, 30-37.
- (12) Chernova, N. A.; Roppolo, M.; Dillon, A. C.; Whittingham, M. S. Layered vanadium and molybdenum oxides: batteries and electrochromics. *Journal of Materials Chemistry* **2009**, *19* (17), 2526-2552.
- (13) Livage, J. Sol-gel chemistry and electrochemical properties of vanadium oxide gels. *Solid State Ionics* **1996**, *86-88*, 935-942.
- (14) Tang, H.; Peng, Z.; Wu, L.; Xiong, F.; Pei, C.; An, Q.; Mai, L. Vanadium-Based Cathode Materials for Rechargeable Multivalent Batteries: Challenges and Opportunities. *Electrochemical Energy Reviews* **2018**, *I* (2), 169-199.
- (15) Li, S.; Xu, Q.; Uchaker, E.; Cao, X.; Cao, G. Comparison of amorphous, pseudohexagonal and orthorhombic Nb<sub>2</sub>O<sub>5</sub> for high-rate lithium ion insertion. *CrystEngComm* **2016**, *18* (14), 2532-2540.
- (16) Kim, J. W.; Augustyn, V.; Dunn, B. The Effect of Crystallinity on the Rapid Pseudocapacitive Response of Nb<sub>2</sub>O<sub>5</sub>. *Advanced Energy Materials* **2012**, *2* (1), 141-148.

- (17) Augustyn, V.; Come, J.; Lowe, M. A.; Kim, J. W.; Taberna, P.-L.; Tolbert, S. H.; Abruña, H. D.; Simon, P.; Dunn, B. High-rate electrochemical energy storage through Li<sup>+</sup> intercalation pseudocapacitance. *Nature Materials* **2013**, *12* (6), 518-522.
- (18) Brandão, R.; Quirino, R.; Mello, V.; Tavares, A.; Peres, A.; Guinhos, F.; Rubim, J.; Suarez, Z. Synthesis, characterization and use of Nb<sub>2</sub>O<sub>5</sub> based catalysts in producing biofuels by transesterification, esterification and pyrolysis. *Journal of The Brazilian Chemical Society JBCS* **2009**, *20* (5), 954-966.
- (19) Anasori, B.; Lukatskaya, M. R.; Gogotsi, Y. 2D metal carbides and nitrides (MXenes) for energy storage. *Nature Reviews Materials* **2017**, *2* (2), 16098.
- (20) Alhabeb, M.; Maleski, K.; Anasori, B.; Lelyukh, P.; Clark, L.; Sin, S.; Gogotsi, Y. Guidelines for Synthesis and Processing of Two-Dimensional Titanium Carbide (Ti<sub>3</sub>C<sub>2</sub>T<sub>x</sub> MXene). *Chemistry of Materials* **2017**, *29* (18), 7633-7644.
- (21) Matthews, K.; Zhang, T.; Shuck, C. E.; VahidMohammadi, A.; Gogotsi, Y. Guidelines for Synthesis and Processing of Chemically Stable Two-Dimensional V<sub>2</sub>CT<sub>x</sub> MXene. *Chemistry of Materials* **2022**, *34* (2), 499-509.
- (22) Foucher, A. C.; Han, M.; Shuck, C. E.; Maleski, K.; Gogotsi, Y.; Stach, E. A. Shifts in valence states in bimetallic MXenes revealed by electron energy-loss spectroscopy (EELS). *2D Materials* **2022**, *9*, 25004.
- (23) Pinto, D.; Anasori, B.; Avireddy, H.; Shuck, C. E.; Hantanasirisakul, K.; Deysher, G.; Morante, J. R.; Porzio, W.; Alshareef, H. N.; Gogotsi, Y. Synthesis and electrochemical properties of 2D molybdenum vanadium carbides solid solution MXenes. *Journal of Materials Chemistry A* **2020**, *8* (18), 8957-8968.
- (24) Wang, L.; Han, M.; Shuck, C. E.; Wang, X.; Gogotsi, Y. Adjustable electrochemical properties of solid-solution MXenes. *Nano Energy* **2021**, *88*, 106308.
- (25) Han, M.; Maleski, K.; Shuck, C. E.; Yang, Y.; Glazar, J. T.; Foucher, A. C.; Hantanasirisakul, K.; Sarycheva, A.; Frey, N. C.; May, S. J.; Shenoy, V. B.; Stach, E. A.; Gogotsi, Y. Tailoring Electronic and Optical Properties of MXenes through Forming Solid Solutions. *Journal of the American Chemical Society* **2020**, *142* (45), 19110-19118.
- (26) Huang, S.; Mochalin, V. N. Hydrolysis of 2D Transition-Metal Carbides (MXenes) in Colloidal Solutions. *Inorganic Chemistry* **2019**, *58* (3), 1958-1966.
- (27) Sui, J.; Chen, X.; Li, Y.; Peng, W.; Zhang, F.; Fan, X. MXene derivatives: synthesis and applications in energy convention and storage. *RSC Advances* **2021**, *11* (26), 16065-16082.
- (28) Clites, M.; Hart, J. L.; Taheri, M. L.; Pomerantseva, E. Chemically Preintercalated Bilayered K<sub>x</sub>V<sub>2</sub>O<sub>5</sub>·nH<sub>2</sub>O Nanobelts as a High-Performing Cathode Material for K-Ion Batteries. *ACS Energy Letters* **2018**, *3* (3), 562-567.
- (29) Pan, D.; Shuyuan, Z.; Chen, Y.; Hou, J. G. Hydrothermal preparation of long nanowires of vanadium oxide. *Journal of Materials Research* **2002**, *17* (8), 1981-1984.
- (30) Husmann, S.; Besch, M.; Ying, B.; Tabassum, A.; Naguib, M.; Presser, V. Layered Titanium Niobium Oxides Derived from Solid-Solution Ti–Nb Carbides (MXene) as Anode Materials for Li-Ion Batteries. *ACS Applied Energy Materials* **2022**, *5* (7), 8132-8142.
- (31) Ma, Q.; Zhang, Z.; Kou, P.; Wang, D.; Wang, Z.; Sun, H.; Zheng, R.; Liu, Y. In-situ synthesis of niobium-doped TiO<sub>2</sub> nanosheet arrays on double transition metal MXene

- $(TiNbCT_x)$  as stable anode material for lithium-ion batteries. *J Colloid Interface Sci* **2022**, *617*, 147-155.
- (32) Yu, H.; Ruan, X.; Wang, J.; Gu, Z.; Liang, Q.; Cao, J.-M.; Kang, J.; Du, C.-F.; Wu, X.-L. From Solid-Solution MXene to Cr-Substituted Na<sub>3</sub>V<sub>2</sub>(PO<sub>4</sub>)<sub>3</sub>: Breaking the Symmetry of Sodium Ions for High-Voltage and Ultrahigh-Rate Cathode Performance. *ACS Nano* **2022**, 16 (12) 21174-21185.
- (33) Tang, H.; Zhuang, S.; Bao, Z.; Lao, C.; Mei, Y. Two-Step Oxidation of Mxene in the Synthesis of Layer-Stacked Anatase Titania with Enhanced Lithium-Storage Performance. *ChemElectroChem* **2016**, *3* (6), 871-876.
- (34) Zhang, R.; Averianov, T.; Andris, R.; Zachman, M. J.; Pomerantseva, E. Liquid Phase Exfoliation of Chemically Prelithiated Bilayered Vanadium Oxide in Aqueous Media for Li-Ion Batteries. *The Journal of Physical Chemistry C* **2023**, 127 (2) 919-929.
- (35) Shi, L.; Ouisse, T.; Sarigiannidou, E.; Chaix-Pluchery, O.; Roussel, H.; Chaussende, D.; Hackens, B. Synthesis of single crystals of V<sub>2</sub>AlC phase by high-temperature solution growth and slow cooling technique. *Acta Materialia* **2015**, *83*, 304-309.
- (36) Lin, H.; Gao, S.; Dai, C.; Chen, Y.; Shi, J. A Two-Dimensional Biodegradable Niobium Carbide (MXene) for Photothermal Tumor Eradication in NIR-I and NIR-II Biowindows. *Journal of the American Chemical Society* **2017**, *139* (45), 16235-16247.
- (37) Azina, C.; Mráz, S.; Greczynski, G.; Hans, M.; Primetzhofer, D.; Schneider, J. M.; Eklund, P. Oxidation behaviour of V<sub>2</sub>AlC MAX phase coatings. *Journal of the European Ceramic Society* **2020**, *40* (13), 4436-4444.
- (38) Shekhirev, M.; Shuck, C. E.; Sarycheva, A.; Gogotsi, Y. Characterization of MXenes at every step, from their precursors to single flakes and assembled films. *Progress in Materials Science* **2021**, *120*, 100757.
- (39) Champagne, A.; Shi, L.; Ouisse, T.; Hackens, B.; Charlier, J.-C. Electronic and vibrational properties of V<sub>2</sub>C-based MXenes: From experiments to first-principles modeling. *Physical Review B* **2018**, *97* (11), 115439.
- (40) Deysher, G.; Shuck, C. E.; Hantanasirisakul, K.; Frey, N. C.; Foucher, A. C.; Maleski, K.; Sarycheva, A.; Shenoy, V. B.; Stach, E. A.; Anasori, B.; Gogotsi, Y. Synthesis of Mo<sub>4</sub>VAlC<sub>4</sub> MAX Phase and Two-Dimensional Mo<sub>4</sub>VC<sub>4</sub> MXene with Five Atomic Layers of Transition Metals. *ACS Nano* **2020**, *14* (1), 204-217.
- (41) 22 Vanadium, Niobium and Tantalum. In *Chemistry of the Elements (Second Edition)*, Greenwood, N. N., Earnshaw, A. Eds.; Butterworth-Heinemann, 1997; pp 976-1001.
- (42) Abello, L.; Husson, E.; Repelin, Y.; Lucazeau, G. Structural study of gels of V<sub>2</sub>O<sub>5</sub>: Vibrational spectra of xerogels. *Journal of Solid State Chemistry* **1985**, *56* (3), 379-389.
- (43) Pomerantseva, E.; Gogotsi, Y. Two-dimensional heterostructures for energy storage. *Nature Energy* **2017**, *2*, 17089.
- (44) Avansi Jr, W.; Ribeiro, C.; Leite, E. R.; Mastelaro, V. R. Vanadium Pentoxide Nanostructures: An Effective Control of Morphology and Crystal Structure in Hydrothermal Conditions. *Crystal Growth & Design* **2009**, *9* (8), 3626-3631.
- (45) Moretti, A.; Maroni, F.; Osada, I.; Nobili, F.; Passerini, S. V<sub>2</sub>O<sub>5</sub> Aerogel as a Versatile Cathode Material for Lithium and Sodium Batteries. *ChemElectroChem* **2015**, *2* (4), 529-537.

- (47) Barbosa, G.; Graeff, C.; Oliveira, H. Thermal annealing effects on vanadium pentoxide xerogel films. *Ecletica Quimica ECLET QUIM* **2005**, *30*.
- (47) Semenenko, D. A.; Itkis, D. M.; Pomerantseva, E. A.; Goodilin, E. A.; Kulova, T. L.; Skundin, A. M.; Tretyakov, Y. D. Li<sub>x</sub>V<sub>2</sub>O<sub>5</sub> nanobelts for high capacity lithium-ion battery cathodes. *Electrochemistry Communications* **2010**, *12* (9), 1154-1157.
- (48) Averianov, T.; Pomerantseva, E. Composite Li-ion battery cathodes formed via integration of carbon nanotubes or graphene nanoplatelets into chemical preintercalation synthesis of bilayered vanadium oxides. *Journal of Alloys and Compounds* **2022**, *903*, 163929.
- (49) Norouzi, N.; Averianov, T.; Kuang, J.; Bock, D. C.; Yan, S.; Wang, L.; Takeuchi, K. J.; Takeuchi, E. S.; Marschilok, A. C.; Pomerantseva, E. Hierarchically structured MoO<sub>2</sub>/dopamine-derived carbon spheres as intercalation electrodes for lithium-ion batteries. *Materials Today Chemistry* **2022**, *24*, 100783.
- (50) Andris, R.; Averianov, T.; Pomerantseva, E. Phase transformation and electrochemical charge storage properties of vanadium oxide/carbon composite electrodes synthesized via integration with dopamine. *Journal of the American Ceramic Society* **2023**, *106* (1), 120-132.
- (51) Li, Y.; Ding, L.; Liang, Z.; Xue, Y.; Cui, H.; Tian, J. Synergetic effect of defects rich MoS<sub>2</sub> and Ti<sub>3</sub>C<sub>2</sub> MXene as cocatalysts for enhanced photocatalytic H<sub>2</sub> production activity of TiO<sub>2</sub>. *Chemical Engineering Journal* **2020**, *383*, 123178.

## **TOC Graphic**

